A REVIEW OF INTA AHS PAF

Eduardo de Miguel[1], Alix Fernández-Renau[1], Elena Prado[1], Marcos Jiménez[1], Óscar Gutiérrez de la Cámara[1], Clara Linés[1], José Antonio Gómez[1], Ana I. Martín[2], and Félix Muñoz[2]

1. INTA, Torrejón de Ardoz, Spain; demiguel(at)inta.es
2. ISDEFE, Madrid, Spain

ABSTRACT

The INTA AHS system has been operational since 2004, having performed over 60 flight campaigns throughout Europe up to the present time. The system is formed by an airborne scanner (AHS), a navigation system, calibration equipment, and a specific processing chain that have been implemented within the INTA airborne data Processing and Archiving Facility (PAF). In this chain, raw data (level 0 product) is transformed to at-sensor radiance (level 1b) and later to georeferenced at-sensor radiance (level 1c). Other processing levels, as atmospherically corrected reflectance, temperature or emissivity (L2b / L2c), can also be produced. The resulting image products are delivered together with radiometric statistics, metadata and quality descriptors according to EUFAR HyQuaPro recommendations. In this paper, details about this processing chain are given. The paper also describes the procedure for in-flight geometric calibration (internal orientation calibration and boresight estimation). Finally, an evaluation of the product accuracy (radiometric, spectral and geometric) is presented, using imagery from different AHS campaigns.

INTRODUCTION

The INTA Airborne Hyperspectral Scanner (AHS) is an 80-band airborne imaging radiometer, developed by ArgonST (USA) and operated by INTA in different remote sensing projects. The AHS is a linescanner with a concept shared with other classical airborne linescanners, like ATM, MIVIS, or MAS. Together with calibration and navigation equipment, auxiliary ground instrumentation and a specific Processing and Archiving Facility (PAF) it forms the INTA AHS system. INTA offers this system as a technological service to public institutions or commercial companies, having performed over 60 flight campaigns since 2004. This system has been presented previously to the users community (1). In this paper, we will review its current status, focusing on its PAF. A twin system, based on the Itres imaging spectroradiometer CASI-1500, is also available, with both instruments nominally used in a tandem configuration. The corresponding INTA CASI PAF is presented in a separate paper (2).

The AHS instrument

The AHS has 63 bands in the reflective part of the electromagnetic spectrum, seven bands in the 3 to 5 micrometre and 10 bands in the 8 to 13 micrometre range. The first element of the optical subsystem is a rotating mirror which directs the surface radiation to a Cassegrain-type telescope. The telescope design includes a so-called pfund assembly, defining a 2.5 mrad instantaneous field of view (IFOV) acting as a field stop, which is therefore unique for all bands, and redirects the radiation to a spectrometer placed above the telescope. In the spectrometer, four dichroic filters are used to split the incoming radiation in five optical ports. Port 1 receives visible and near-infrared (VNIR) wavelengths; Port 2a, for a single band at 1.6 micrometres; Port 2, for short wave infrared (SWIR); Port 3, for mid-infrared (MIR), and Port 4, for thermal infrared (TIR). For each of these ports, a grating disperses the radiation and a secondary optical assembly focuses it onto an array of detectors which defines the final set of (contiguous) spectral bands. Table 1 summarises the AHS spectral configuration; it is important to note that bands 22 to 24 and 60 to 63 are located inside regions with strong atmospheric interference and therefore show a very low signal-to-noise ratio (*SNR*). The main electro-optical parameters of AHS are summarised in Table 2.

DOI: 10.12760/01-2014-1-03

Table 1: AHS spectral configuration (from 2006 on).

	PORT 1 VIS+NIR	PORT 2A SWIR	PORT 2 SWIR	PORT 3 MIR	PORT 4 TIR (LWIR)
coverage (micrometre)	0.43 – 1.03	1.55 – 1.65	1.90 – 2.55	3.30 – 5.40	8.00 – 12.70
bandwidth (FWHM)	28 nm	90 nm	18 nm	300 nm	450 nm
bands	20	1	42	7	10

Table 2: Main characteristics of AHS.

Telescope optical design	Scan mirror plus cassegrain-type reflective optics, with a single IFOV determining field stop (*Pfund assembly*)
FOV (Field Of View) IFOV (Instantaneous FOV)	90° 2.5 mrad
Ground Sampling Distance	2.1 mrad (0.12 degrees)
Scan rates	12.5, 18.75, 25, 35 revolutions per second, with corresponding ground sampling distances at nadir from 7 to 2.5 m at flight altitudes from 2700 to 1000 m
Electronic chain	gain level from ×0.25 to ×10, anti-alias filtering, 12 bits to sample the analogue signal
Samples per scan line	750 pixels/line plus reference sources data
Reference sources	two controllable thermal black bodies within the field of view, set to a temperature range from -15ºC to +25ºC with respect to scan head heat sink temperature
Spectrometer	four dichroic filters to split radiation into four optical ports and diffraction gratings within each port; detectors: Si array for VIS/NIR focal plane, InSb and MCT arrays, cooled in N2 dewars, for SWIR, MIR and TIR focal planes

AHS has two blackbodies (with size > IFOV) that are observed at the start and end of each scan-line, respectively. These blackbodies (BB1 and BB2) are thermally controlled and monitored; according to instrument specifications, they have an emissivity above 0.95 in the MIR and TIR regions and a reflectivity <1% in the VNIR-SWIR range. Therefore, for each AHS band and image line, two "dark and thermal reference" pixels are available. As dark reference pixels (applicable to VNIR and SWIR), BB1 and BB2 duplicate the same information, whereas the thermal reference (applicable to MIR and TIR regions) consists in a cold reference pixel (BB1) and a hot reference pixel (BB2).

Calibration

The radiometric calibration of the VNIR and SWIR detectors is achieved illuminating the system with a uniform and known radiance source. This source is a 1.01 metres (40 inches) diameter integrating sphere from Labsphere® with ten halogen lamps placed inside of it. The internal surface of the sphere is covered with a high diffuse reflective coating, Spectraflect, in which the light coming from the lamps is reflected. As a result, a uniform illuminance beam comes out through the circular aperture of the sphere. The integrating sphere can be configured turning on one or several lamps, and the relevant configurations are calibrated in radiance by Labsphere® under traceable NIST reference.

Thermal infrared ports (MIR and TIR) are calibrated in the laboratory by means of an extended area blackbody source set at a known temperature.

Radiometric calibration of the detectors provides also *NEdL* and *NEdT* values which are routinely monitored.

The main component of the spectral calibration system is a monochromator used to illuminate the AHS with steps of 0.1 nm and a bandwidth around 5 nm. The relative instrument response at the different wavelengths is used to build a responsivity curve for each band. The curves are nearly Gaussian, but anyhow the detailed spectral responsivity is available to users of AHS images.

The AHS sensor includes an integrated Applanix POS/AV navigation system, which relies upon a GPS and an Inertial Measurement Unit (IMU) for accurate determination of the instrument position and orientation. Synchronization of AHS and POS/AV measurements is performed with a dedicated synchronization signal issued by AHS precisely at the time of acquisition of each image row centre pixel and recorded by POS/AV as an "event".

Geometric calibration is aimed at measuring the boresight angles, i.e., the angles between POS/AV IMU axis and sensor (image) axis. The IMU is fixed to the sensor body, but its reference system is slightly rotated with respect to the sensor (and image) coordinate system. This requires the relation of both reference systems to be determined in terms of roll, pitch and yaw misalignments (boresight angles). The boresight angles are computed with an empirical approach implemented in PARGE (3) and based on Ground Control Points (GCPs) collected at a calibration field. Most of them are artificial (white-plastic) sub-pixel targets. A differential GPS field campaign is performed to collect the cartographic coordinates of these GCPs.

The estimated boresight angles are valid as long as the sensor-IMU-GPS locations do not change their relative positions, and therefore usually for a complete flight season, as reported for other sensors (4).

INTA AHS products

The INTA Remote Sensing Laboratory performs the processing of the images acquired with the AHS. Different products are available to the users according to the processing level, following the classical categories L1a, L1b, L1c, L2. Table 3 defines each possible product.

Table 3: INTA-AHS products.

Level 1 image product	L1a (filename code: L0R00)	**Raw product** – INTA-AHS L1a images, 753 values per line (including marker bit and digital numbers for two onboard reference black bodies). Image product with 80 bands in BIL format + ENVI header and with ancillary information, statistics and radiometric calibration coefficients.
	L1b L10020/L00120	**User product** - INTA-AHS L1b images - georeferenceable calibrated at sensor radiance, in BSQ format + ENVI header, usually with an Input Geometry Map file (IGM) attached for georeferencing.
	L1c L10022/L00122	**User product** - INTA-AHS L1c images - georeferenced calibrated at sensor radiance, in BSQ format + ENVI header.
Level 2 image product	L2b L20020/L20120	**User product** - INTA-AHS L2b images – georeferenceable hemispherical-directional reflectance factor and kinetic temperature, in BSQ format + ENVI header, usually with Input Geometry Map file (IGM) attached for georeferencing.
	L2c L20022/L20122	**User product** - INTA-AHS L2c images - georeferenced hemispherical-directional reflectance factor and kinetic temperature in BSQ format + ENVI header.

DESCRIPTION OF THE PROCESSING CHAIN

In the INTA-AHS PAF, in-house developed tools (based mainly on MATLAB and IDL) and some pieces of commercial software are integrated in an operational workflow. The integration is not designed for a fully automatic operation, but rather for a modular use: each step in the workflow must be configured manually and launched by an operator, and then runs alone for the specified dataset. Figure 1 presents an overview of the INTA-AHS PAF operational flow; details are given in the following sections.

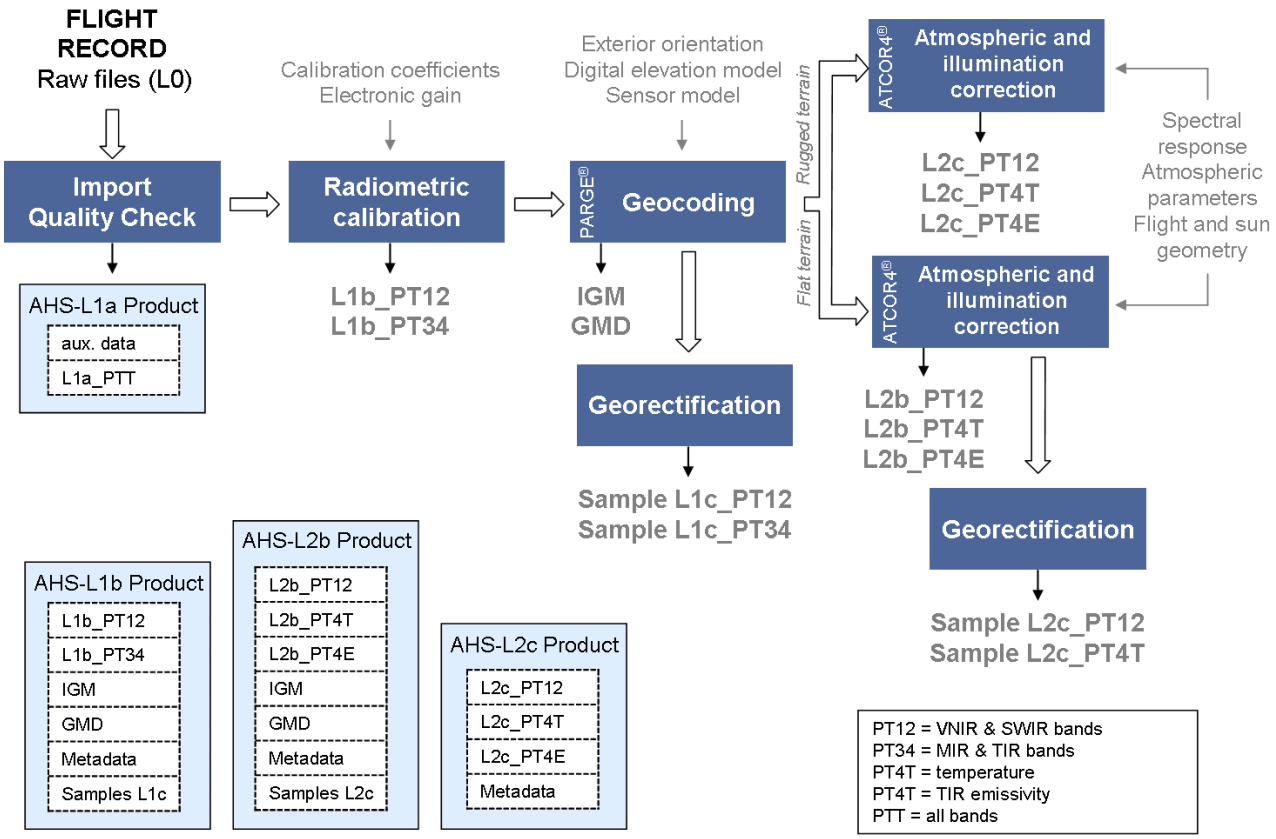

Figure 1: Overview of the INTA-AHS PAF operational workflow.

Data import

The first step, data import, is based on an importing utility provided by the instrument vendor. This utility simply unpacks source data files and formats them in ENVI compatible files. No data transformation is performed at this level. An in-house tool is used to perform raw data quality checks, file renaming and ENVI header update. The corresponding product, L1a, is useful only to researchers who would like to work from the raw image data, and is only delivered on request.

Radiometric calibration

Radiometric calibration transforms the image values from digital number to at-sensor radiance (Ls) for VNIR/SWIR region according to a linear model:

$$Ls_{i,j,k} = \frac{cc_k}{g_k} \cdot (DN_{i,j,k} - DNbb_{i,k})$$

The subscripts {*i*,*j*,*k*} correspond to image {row, column, band} respectively. *cc* is the calibration coefficient, *g* an adjustable electronic gain, *DN* the raw Digital Number and *DNbb* the average of both blackbodies data over a 15-row moving window centred in row "*i*". Note that in this linear model the slope depends on laboratory measurements, but the offset is estimated from the actual image. It is possible to introduce an empirical correction factor to *cc* for specific campaigns. This factor is usually aimed to account for the eventual degradation in sensor response as a function of the time elapsed since the last calibration, and its value can be estimated from ground data or interpolation between pre- and post-flight season calibration coefficients. This value is chosen by the operator and is reported to the user in the statistics and calibration information file.

For MIR and TIR bands, radiometric calibration transforms the image values from digital number to at-sensor radiance (*Ls*) according to:

$$Ls_{i,j,k} = \frac{DN_{i,j,k} - DNbb1_{i,k}}{DNbb2_{i,k} - DNbb1_{i,k}} \cdot (Lbb2_{i,k} - Lbb1_{i,k}) + Lbb1_{i,k}$$

Again, the subscripts {*i*,*j*,*k*} correspond to image {row, column, band} respectively. *DN* is the raw Digital Number and *DNbbx* the average of the blackbody recorded values over a 15-pixel moving window, but this time *BB*1 and *BB*2 are not averaged but separate parameters of the model. *Lbb*1 and *Lbb*2 are the *BB*1 and *BB*2 emitted radiances computed from their temperature (as monitored in flight) and effective emissivity. Note that in this linear model both the slope and the offset are estimated from the actual image (blackbody reading).

Geolocation and IGM

The geolocation of airborne linescanner data based on direct georeferencing techniques requires the accurate determination of the position and attitude of the scanning instrument. These parameters are derived from the continuous acquisition data with combined GPS and IMU measurements. The Applanix POS/AV system includes a post-processing software suite called POSPac-MMS (5) to retrieve the external orientation parameters.

The geolocation (geocoding) of each AHS pixel is performed from the exterior orientation information, the digital elevation model (DEM) and a detailed sensor model using the direct georeferencing code PARGE. The basic output of the process is an Input Geometry file (IGM) for each image. IGM image files denote the UTM Easting and Northing values derived by the geocoding process for each original image pixel. The IGM files have the same spatial size as the AHS L1b imagery and contain the geolocation information for each original pixel.

Resampling

The AHS orthorectified data cube can be created in different ways depending on the resampling algorithm used. In our nominal processing chain we use the ENVI routine Georeference from IGM with the optimum pixel size selected according to our knowledge of the campaign. This option works from the input geometry by creating a so-called geometry lookup table (GLT) file. The GLT file contains the sample and line that each pixel in the output image came from in the input image. The GLT algorithm is applied then only to a subset of visible bands (allowing either a true colour or infrared colour composite), and a single thermal band. These georectified bands are delivered to the user mainly as a quicklook to display the expected output of the orthorectification process. The user is expected to choose an own resampling algorithm and output pixel size to produce the complete orthorectified data cube from the delivered IGM with the support of that georectified quicklook.

L2 products

Atmospheric and illumination correction is performed with ATCOR4 (6), which is a LUT-based implementation of MODTRAN5 targeted for airborne remote sensing data. Following the definitions in (7), the physical quantity estimated by ATCOR4 for solar bands is the Hemispherical-Directional Reflectance Factor (*HDRF*) of the observed surface.

For ATCOR4 configuration, atmospheric water vapour is either estimated from external atmospheric data or retrieved from estimations made with ATCOR4 from simultaneous CASI images. Visibility and aerosol type are estimated from external atmospheric data, although ATCOR4 enables their estimation from dense-dark-vegetation image spectral statistics.

To compute surface temperature from ATCOR4, INTA uses a monoband algorithm, in which emissivity is fixed *a priori* (either a constant value or a set based on surface classes). For specific projects, temperature/emissivity separation algorithms are used. In this case, the characteristics of the input image (time of the day, scene composition) are considered together with the user's needs in order to choose the best procedure from those available in ATCOR4.

In specific campaigns, INTA acquires and processes ASD FieldSpec-3 spectra with the goal of supporting the generation of L2 products. These spectra could be used either as inputs to ATCOR4 including functionalities for in-flight calibration and fine-tuning of atmospheric parameters, or as ground truth for validation of the obtained reflectance products.

Metadata and quality reporting

A first evaluation of the quality of acquired images is performed in near-real time during the flight campaign (8). This quick quality assessment is required to agree with the user on the successful completion of the planned flight programme.

Metadata elements and quality parameters for higher level products are generated following the recommendations given by the EUFAR-HyQuaPro activity (9). Accordingly, we systematically attach to each image product a text file with a pre-defined set of fields reporting image acquisition parameters and processing, lineage and contact information. This text file is generated by specific IDL functions.

In addition to these quality descriptors, image statistics are computed per band and provided to the user in a specific text file. This statistics file contains:

1) Calibration parameters: calibration coefficients, gain, reference blackbodies temperature.
2) Blackbody statistics: the short-term standard deviation of the BBs is taken as an estimation of the AHS instrumental noise (note that, along with instrumental noise, shot noise is included in the case of MIR and TIR).
3) Scene statistics: saturated or missing pixels, scene average signal and an approximation to signal-to-noise ratio. Note that the value reported under *SNR* is the scene average times blackbody variability, and so is not a rigorous *SNR* figure; but on the other hand, is a sufficient approximation to actual *SNR* and is more robust and reliable than other approximations.

Finally, specific information is provided on the geometrical features of each pixel. These are the so-called geometric metadata (GMD), which are reported as layers in an auxiliary file, with the same pixel-column dimensions as the radiometric data but with the following info as bands:

- View (scan) zenith angle
- View absolute azimuth
- Pixel distance (= view path length)
- Orthometric terrain height
- Actual ground *IFOV* across-track
- Actual ground *IFOV* along-track

These values are computed following rigorous models and using actual flight, sensor and terrain information. This is an essential file to take account of several effects that appear in the aerial remote sensing imagery. For example, the area contributing to each pixel (ground *IFOV*) is an important parameter. In the case of images acquired from aircraft over mountainous terrain this parameter is highly variable (Figure 2a), therefore, knowing its distribution across both the length and width of the image is very convenient (10).

PRODUCTS QUALITY

Radiometric quality

A simple and generic evaluation of the radiometric accuracy of AHS radiometric measurements in ports 1 and 2 is not possible. It depends on a number of variables, chiefly the amount of operation hours since the applicable laboratory calibration. The estimated radiometric accuracy for a specific data set can be provided to the user under request.

For ports 3 and 4 the uncertainty is only limited by the accuracy of the estimation of onboard blackbodies output radiance, used for computing the calibration line. The study of the measured BB1 and BB2 temperatures along single images and during flight sessions shows no unexpected values or significant trends, which supports the assumption that temperatures reported are correct and reliable. BB emissivity is well known; however, as the value is close to 0.96, the BB-leaving radiance includes a non-negligible contribution from reflected thermal radiation, which is very diffi-

cult to estimate (it depends on emissivity and temperature of the different elements in the AHS scan head and of the view factor of BBs for each element). To account for this contribution, an effective emissivity of 0.975 is nominally used for MIR and TIR bands calibration. Nevertheless, different tests and simulations have shown that an accuracy better than 2% of the measured radiance *Ls* is to be expected for standard surface temperatures even with this reflected contribution uncertainty. In Figure 2b, the variation in estimated *Ls* is plotted as a function of the input digital count for a range of likely values of the environmental thermal radiation: the maximum variation is 0.6% of the input radiance. A similar study has been reported for MAS (11); however, for MAS the main source of error was supposed to be the difference between actual BB temperature and the reported value. It is important to note that MAS was flown in ER2 at an altitude of around 20 km, where environmental cooling of blackbodies is severe.

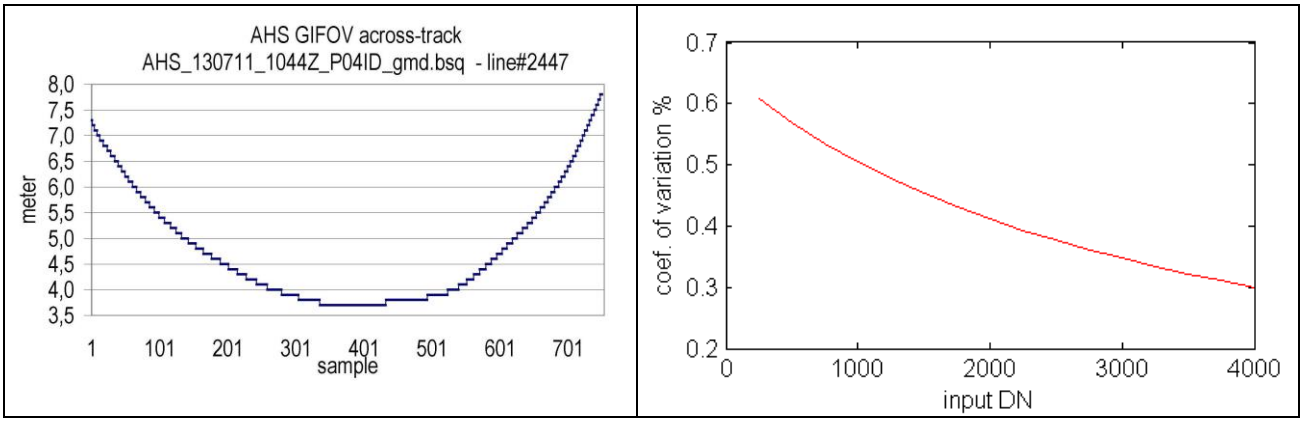

Figure 2a (Left): value of ground IFOV (metres) for the 750 across-track pixel in an image line acquired over a hilly area. Figure 2b (Right): relative standard deviation (coefficient of variation) of the set of values for Ls computed from the DN considering a range of reflected thermal radiation. The set of values of Ls corresponds to scan head emissivities from 0.45 to 0.95 and temperatures from 275 to 295 K. AHS blackbody emissivity has been set to 0.96, as reported by the instrument documentation.

As stated above, an estimation of noise and *SNR* for each image is performed systematically. Figure 3 shows results for *SNR* for data acquired in 2012. The figure shows that *SNR* in Ports 1 and 2 is very good. In Ports 2, 3 and 4, the bands located in the edges (where atmospheric transmission is poor) show a significantly lower *SNR*; finally, the defective detectors 44 and 46 show a low *SNR*.

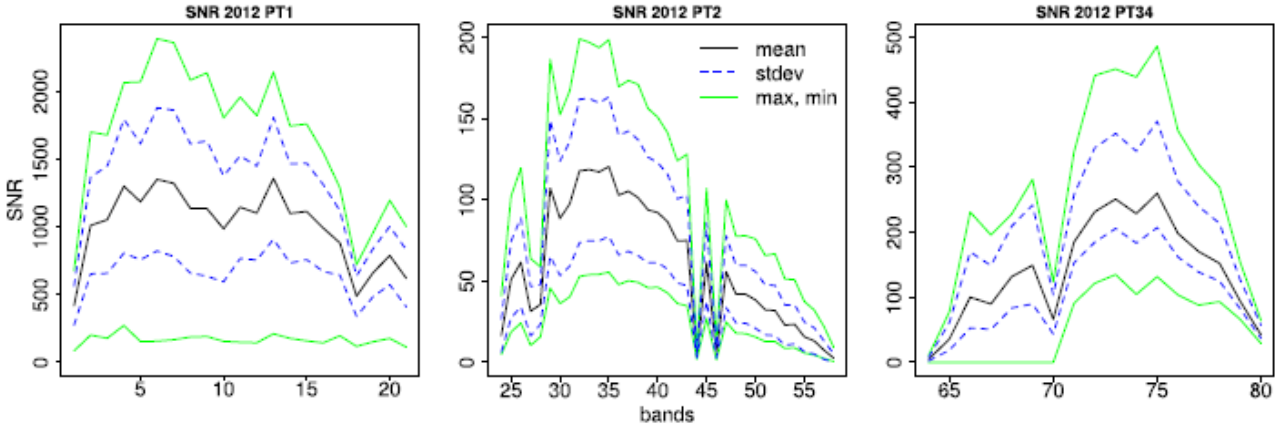

Figure 3: Statistics for Signal-to-Noise Ratio (SNR) for the AHS images acquired during 2012.

A significant point is the effect of noise in the emissivity retrieved from AHS thermal bands. Although the noise amplitude in these bands is fairly low, with a standard deviation below 0.3°C for most bands, other noise characteristics are rather negative for noise reduction techniques. First, this noise is not stationary, but has a strong spatial correlation; but, on the other hand, there is no specific frequency associated to the noise, so that it is difficult to filter it out using Fourier space techniques. Secondly, it shows a non-negligible spectral correlation, reducing the efficiency of the

Minimum Noise Fraction transform and similar algorithms to remove noise. As a result, emissivity retrievals from AHS images sometimes show a noisy aspect (12).

Spectral accuracy

The design of the AHS spectrometer avoids spectral smile or similar effects. At the same time, it is fairly robust against spectral shifts (Figure 4a). However, an eventual spectral miscalibration could occur due to an unusual instrument stress during the flight season. A specific tool has been set up (13) to perform spectral-shift checks in operational images and is ready to be used whenever an anomalous spectral behaviour is detected. For port 2, with the narrower bands, the tool available in ATCOR4 is also used. Figure 4a shows the results obtained with these tests for two flight campaigns performed in 2013 on the same test site (Cazalegas, Toledo); the applicable laboratory spectral calibration was performed in March 2013. As expected, the estimated spectral shifts are negligible for the flight closer to the laboratory calibration and minor (less than 15% of the bandwidth) for the second flight.

Cartographic accuracy

On flat terrain, the main contributor to the error budget is the uncertainty in the boresight angles. Other minor sources of error are inherited from PARGE limitations; these minor error sources are not expected to account for more than 1/2 pixel uncertainty in the image edges, and less than this in the nadir. Overall, and as confirmed during dedicated studies, we have estimated that the usual absolute geolocation error is isotropic and below 1 pixel. In rugged terrain, DEM resolution and accuracy become major contributors to the error budget.

To check the actual absolute cartographic accuracy in a specific image, the usual way is to collect ground control points (GCPs). This is not done systematically, but only for several campaigns for monitoring purposes or specific requirements. As an example, for the CEOSS-2013 campaign the RMSE-2D computed from easting (X) and northing (Y) differences (shown in Figure 4b) is 1.5 m.

24-04-2013 (Cazalegas, Toledo)		
Pass	Spectral shift	St dev
P01I1	-0.21	0,17
P01I2	-0.24	0.14
P02	-0.18	0.29
P03	-0.19	0.24
P04	-0.19	0.40

11-07-2013 (Cazalegas, Toledo)		
Pass	Spectral shift	St dev
P01	-2.41	0.36
P02	-2.37	0.35
P03	-2.40	0.13
P04	-2.45	0.12
P05	-2.33	0.10
P06	-2.39	0.29

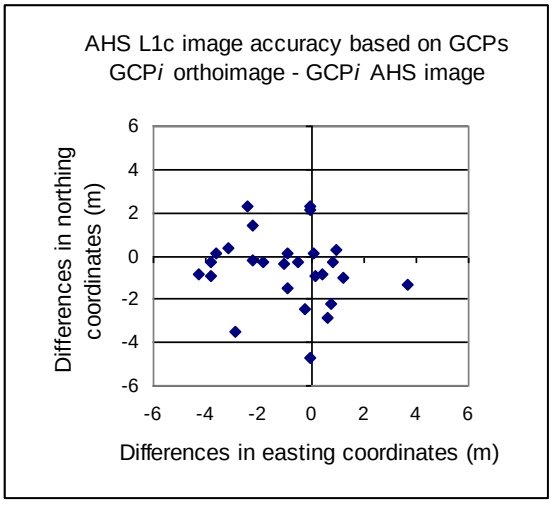

Figure 4a (Left): Spectral shift (i.e., difference between the nominal band centre and the estimated one) in AHS port 2 as reported by ATCOR4 for two 2013 flight campaigns, for which the applicable laboratory spectral calibration was performed in March 2013. Eight target surfaces have been used as input to estimate the spectral shift for each image. Figure 4b (Right): AHS horizontal accuracy assessment using GCPs. The plot shows the differences between each of the 25 GCP coordinates in an orthophoto of higher accuracy and in AHS L1c images. AHS pixel size at nadir is 4 metres. RMSEx=2.1 m / RMSEy=1.7 m / RMSE-2D=1.5 m.

A complementary evaluation of geometric performance is the image-to-image registration, which reports the geolocation relative accuracy. A specific tool is available for this purpose. The tool is based on detecting misregistration in subsets covering the whole image. For each subset, the correlation in intensity level between the nominal L1c output and different cases, each one with an intentional shift in the geolocation, is computed; the shift (or no shift) producing the highest correlation is selected. The representation of the misregistration pattern allows uncovering boresight or exterior orientation errors. This tool is used if anomalies are suspected; in AHS standard imagery, the pattern shows that misregistration is below 1 pixel, and image-to-image analysis can be performed down to resampling limitations.

FUTURE WORK

The processing chain described in the previous sections is fully operational, and it is planned to maintain its basic elements in the near future with only minor modifications. Future work will therefore be aimed at extending its capabilities, and three topics are currently being considered:

- Spectral stray light estimation and correction.
- The improvement of the temperature/emissivity separation algorithms, implementing a procedure optimized to the AHS features and as robust as possible against noise.
- The implementation of specific procedures for the estimation of reflectance in forest canopies (a frequent target of hyperspectral remote sensing studies), where the observation and illumination angles are not defined by the terrain model and where the number of shadowed pixels is significant, but they cannot be detected with simple methods.

REFERENCES

1 Fernández-Renau A, J A Gómez & E de Miguel, 2005. The INTA AHS system. In: SPIE 5978 - Sensors, Systems, and Next-Generation Satellites IX, edited by R Meynart, S P Neeck & H Shimoda (SPIE, Bruges), 8 pp.

2 de Miguel E, A Fernández-Renau, E Prado, M Jiménez, Ó G de la Cámara, C Linés, J A Gómez, A I Martín & F Muñoz, 2014. The processing of CASI-1500I data at INTA PAF. EARSeL eProceedings, 13(1): 30-37

3 Schläpfer D & R Richter, 2002: Geo-atmospheric processing of airborne imaging spectrometry data. Part 1: Parametric Orthorectification. International Journal of Remote Sensing, 23(13): 2609-2630

4 Holzwarth S, R. Müller & C Simon, 2005. Determination and monitoring of boresight misalignment angles during the hymap campaigns HYEUROPE 2003 and HYEUROPE 2004. In: 4th EARSeL Workshop on Imaging Spectroscopy - New quality in Environmental Studies, edited by B Zagajewski, M Sobczak & M Wrzesień (EARSeL and Warsaw University, Warsaw) 91-100

5 Hutton J, A Ip, T Bourke, B Scherzinger, N Gopaul & P Canter, 2008. Tight integration of GNSS post-processed Virtual Reference Station with inertial data for increased accuracy and productivity of airborne mapping. The International Archives of the Photogrammetry, Remote Sensing and Spatial Information Sciences, 37(B5): 829-834

6 Richter R & D Schläpfer, 2002. Geo-atmospheric processing of airborne imaging spectrometry data. Part 2: Atmospheric/Topographic correction. International Journal of Remote Sensing, 23(13): 2631-2649

7 Schaepman-Strub G, M E Schaepman, T H Painter, S Dangel & J V Martonchik, 2006. Reflectance quantities in optical remote sensing—definitions and case studies. Remote Sensing of Environment, 103: 27-42

8 Gutiérrez de la Cámara O, F Muñoz, J A Gómez, A Fernández-Renau, E de Miguel, C Doñamayor & M Jiménez, 2013. Control de calidad de datos AHS en vuelo. In: XV Congreso de la Asociación Española de Teledetección, edited by A. Fernández-Renau & E. de Miguel (INTA, Madrid)

9 Holzwarth, S, M Bachmann, M Freer & M Hofmann, 2011. Standards for airborne hyperspectral image data. In: Proceedings of the EARSeL 7th SIG-Imaging Spectroscopy Workshop, 7 pp.

10 González Lagos M, E de Miguel Llanes, M Jiménez Michavila & E Prado Ortega, 2012. Pérdida y redundancia de información en imágenes aeroportadas georreferenciadas sobre zonas de montaña. In: XV Congreso Nacional de Tecnologías de la Información Geográfica, edited by J Martínez Vega & P Martín Isabel (CSIC, Madrid) 563-572

11 Moeller C C, P S Grant, D D LaPorte, L E Gumley, P Hajek, W P Menzel, J S Myers & S White, 1996. Blackbody emissivity considerations for radiometric calibration of the MODIS Airborne Simulator (MAS) thermal channels. In: SPIE 2820 – Earth Observing System, edited by W L Barnes (SPIE, Denver), 44

12 Jimenez-Muñoz J C, J A Sobrino & A R Gillespie, 2012. Surface Emissivity Retrieval From Airborne Hyperspectral Scanner Data: Insights on Atmospheric Correction and Noise Removal. Geoscience and Remote Sensing Letters, IEEE, 9(2): 180-184

13 De Miguel E, R Rodríguez & O Gutiérrez de la Cámara, 2010. Monitoring the spectral accuracy of AHS images. In: 3rd International Symposium on Recent Advances in Quantitative Remote Sensing, edited by J A Sobrino (Universidad de Valencia) 461-465